nature communications

Article

https://doi.org/10.1038/s41467-026-77679-7

Colossal and fully reversible barocaloric effect for sustainable cooling in a pressure-sensitive spin-crossover complex

Received: 11 June 2025

Accepted: 26 August 2026

Published online: 15 September 2026

Check for updates

Yue Kan[1,2,16], Shuo Meng[3,16], Si-Wei Yan[1,2,16], Rui-Xin Li[4], Qing-Zhen Huang[5,6], Yue-Xing Zhang[7], Yang Ren[8], Zi-Long Zhao[9], Ivan da Silva[10], Li-Jin Wang[11], Chang-Qing Jin[1,2], Zheng-Ying Tian[1,2], Han Liang[3], Yuan-Sha Chen[1,2], Quan-Jun Li[4], Jing Wang[1,2] ✉, Yun-Zhong Chen[1,2], Dao-Peng Zhang[3] ✉, Jia Yan Law[12], Victorino Franco[12], Oliver Gutfleisch[13], Feng-Xia Hu[1,2] ✉ & Bao-Gen Shen[1,2,14,15] ✉

Barocaloric refrigeration has great potential to replace traditional vapor-compression systems, which are conspicuously harmful to the environment. Investigating barocaloric effect driven by a practical pressure remains challenging. Here, we report that the spin-crossover (SCO) complex $Fe(PC4HH)_2$ (PC4HH = 4-hydroxy-N′-((pyridin-2-yl)-methylene)-benzohydrazide) exhibits a colossal and reversible barocaloric entropy change (ΔS_r, up to ~125 $J \cdot K^{-1} \cdot kg^{-1}$) under a small pressure ~7.5 MPa owing to the extremely high pressure sensitivity of transition temperature (dT_c/dP, 5.56 K/MPa). Synchrotron radiation PXRD demonstrate that the source of the enhanced ΔS_r and the ultra-large dT_c/dP come from the gas (air) adsorption of pressure transimitting medium. The superior pressure sensitivity and outstanding barocaloric performance provide a feasible way to exploit novel barocaloric materials by utilizing the complexation properties of SCO materials with gas.

With the constant civilization and development of society, resources are being consumed at an astonishing speed. Refrigeration, which uses nearly 20% of the global electricity supply every year, is definitely a cause of the resource crisis[1–4]. However, refrigeration is essential in our lives, from temperature control of high-tech devices such as chips, computers, and consumer electronics to air conditioners and refrigerators. The current refrigerants used in large-scale air-conditioners and refrigerators are mostly harmful gases like hydrofluorocarbons, which have global warming potentials exceeding 2000 times that of CO_2 and hence are unfriendly to our planet[5,6]. To reduce the emission

[1]Beijing National Laboratory for Condensed Matter Physics, Institute of Physics, Chinese Academy of Sciences, Beijing, PR China. [2]School of Physical Sciences, University of Chinese Academy of Sciences, Beijing, PR China. [3]College of Chemistry and Chemical Engineering, Shandong University of Technology, Zibo, PR China. [4]State Key Laboratory of Superhard Materials, International Centre of Future Science, Jilin University, Changchun, PR China. [5]Songshan Lake Materials Laboratory, Dongguan, Guangdong, PR China. [6]Spallation Neutron Source Science Center, Dongguan, PR China. [7]Shandong Provincial Key Laboratory of Monocrystalline Silicon semiconductor Materials and Technology, College of chemistry and chemical engineering, Dezhou University, Dezhou, China. [8]Department of Physics, JC STEM Lab of Energy and Materials Physics, City University of Hong Kong, Hong Kong, China. [9]Shanghai Advanced Research Institute, Chinese Academy of Sciences, Shanghai, PR China. [10]ISIS Neutron and Muon Source, Science and Technology Facilities Council, Rutherford Appleton Laboratory, Didcot, UK. [11]Institute of Advanced Materials and Technology, University of Science and Technology, Beijing, PR China. [12]Multidisciplinary Unit for Energy Science, Dpto. Física de la Materia Condensada, Universidad de Sevilla, Sevilla, Spain. [13]Institute of Materials Science, Technical University of Darmstadt, Darmstadt, Germany. [14]Ganjiang Innovation Academy, Chinese Academy of Sciences, Ganzhou, China. [15]Ningbo Institute of Materials Technology & Engineering, Chinese Academy of Sciences, Ningbo, China. [16]These authors contributed equally: Yue Kan, Shuo Meng, Si-Wei Yan. ✉e-mail: wangjing@iphy.ac.cn; dpzhang73@126.com; fxhu@iphy.ac.cn; shenbg@iphy.ac.cn

of such harmful gases and achieve the carbon neutrality target, new types of environmentally benign and safe refrigerants and cooling technologies need to be developed[7].

Solid-state refrigeration based on caloric effects has emerged in response to such needs[8]. The past few years have witnessed rapid development in this research area of magnetocaloric effect (MCE)[9–13], electrocaloric effect (ECE)[14–17], elastocaloric effect (eCE)[18–20], and barocaloric effect (BCE)[21–24]. Particularly, the discovery of colossal BCE in plastic crystals was a milestone, with a barocaloric entropy change ΔS ~ 500 $J{\cdot}K^{-1}{\cdot}kg^{-1}$ for neopentyl glycol in 2019[25,26], and new findings were demonstrated in ionic plastic crystals with ΔS ~ 200 $J{\cdot}K^{-1}{\cdot}kg^{-1}$ six years later[27], which has stimulated interest in this field. Moreover, a larger barocaloric energy change of ~720 $J{\cdot}K^{-1}{\cdot}kg^{-1}$ was discovered in *n*-alkanes associated with solid–liquid phase transition[28]. However, despite their large entropy changes, it is still unclear whether these materials can be practically used because the pressure required to achieve these values is usually large. The pragmatically related properties, the reversible entropy change (ΔS_r) and reversible adiabatic temperature change (ΔT_r), are generally very small under low pressure (<50 MPa) owing to considerable hysteresis and sluggish pressure sensitivity (small dT_c/dP value)[29], even though the material itself has a large entropy change.

In 2016, spin-crossover (SCO) materials were proposed as potential candidates for BCE materials[30]. SCO complexes are a huge family with diverse structure types[31–40]. They can contain one, two, or more central metal ions in the SCO unit, such as a single Fe ion or two Fe ions or one Co and one Mn ion, and the ligands connecting the metal cores are also diverse (e.g., N_6, N_2O_4, or $N_2S_2O_2$). The change of the spin state (SCO) of metal ions can be realized by energy gap variation. Taking the case of a single transition metal core (Fe^{2+}) as an example (Fig. 1a), the crystal fields emanating from the ligands split the *d* orbital into t_{2g} and e_g orbitals, and the energy gap (Δ) between the t_{2g} and e_g orbitals determines the spin state of the metal ion. When the Δ originating from ligands is larger than the electron pair energy (E_{pair_energy}), three pairs of electrons with opposite spin directions occupy the t_{2g} orbitals, resulting in a low-spin (LS) state (i.e., the total spin quantum number $S = 0$, left part of Fig. 1a). While the ligands' environments enable the Δ to be smaller than E_{pair_energy}, the electrons remain as far from each other as possible, leading to a high-spin (HS) state with $S = 2$ (right part of Fig. 1a). Accompanying the SCO in the split *d* orbitals, the induced phonon/lattice change along with magnetic contributions leads to considerable calorics[41–52]. Differing from the mechanism of large BCE in plastic crystals[25,27,29], SCO complexes provide an ideal platform for exploring ultra-sensitive barocaloric materials, considering the sensitivity of Δ to the ligands' environments, stress, and diverse connections.

Herein, we report the SCO complex $Fe(PC4HH)_2$ (**1**, PC4HH = 4-hydroxy-*N*′-((pyridin-2-yl)-methylene)-benzohydrazide) showing an

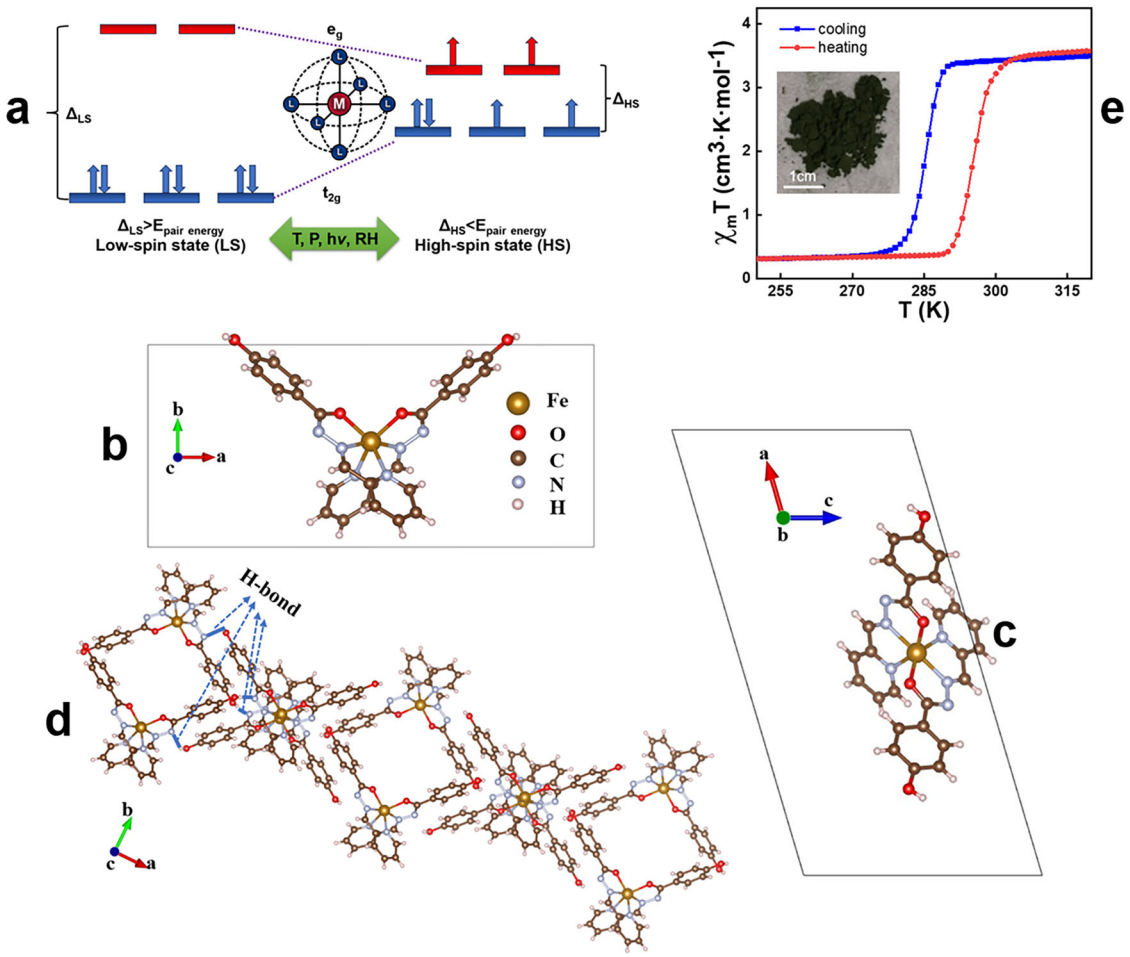


Fig. 1 | Structure of complex 1. a Illustration of the spin-crossover (SCO) transition. Mononuclear structure of complex **1** in the **b** *ab* and **c** *ac* planes. **d** Two-dimensional supramolecular structure formed by the intermolecular hydrogen bond interactions along the *ab* plane. Part of O–H…N hydrogen bonds are indicated by blue arrows in the left most. Atom Color: Fe, gold; O, red; C, brown; N, gray; H, pink. **e** Plot of the molar magnetic susceptibility ($\chi_m T$) versus the temperature (*T*) during heating and cooling with a temperature scanning rate of 1 K/min measured by a superconducting quantum interference device (SQUID) under a magnetic field of 1000 Oe. The insert shows the morphology of the dark-green sample powder.

extremely high-sensitivity pressure response (dT_c/dP ~ 5.56 K/MPa at $P < 5$ MPa and 0.957 K/MPa at $P > 20$ MPa). The saturated entropy change across the phase transition is ΔS ~ 125 $J{\cdot}K^{-1}{\cdot}kg^{-1}$, and it reaches and then remains stable under pressures above 7.5 MPa, bringing about an adiabatic temperature change of ΔT_{ad} ~ 30 K. Because of this high pressure sensitivity, the phase transition can be driven by a very small pressure of ~7.5 MPa and gives rise to a reversible barocaloric entropy change as much as ΔS_r ~ 125 $J{\cdot}K^{-1}{\cdot}kg^{-1}$ at ~300 K, which empowers practical potential for sustainable cooling rather than only the theoretical potential of most other BCE materials.

Results

Basic structure and magnetic properties of 1

We synthesized sample **1** as a dark-green polycrystalline powder (see the Methods for details). The structure of the HS state has been previously determined to be monoclinic with a space group of $C\,2/c$ and lattice parameters of $a = 22.801(5)$ Å, $b = 9.917(2)$ Å, $c = 11.686(2)$ Å, $\alpha = \gamma = 90°$, and $\beta = 106.47(3)°$ using single-crystal X-ray diffraction (SC-XRD)[53]. The asymmetric unit of **1** is a typical neutral mononuclear structure with the octahedral Fe^{2+} ion located in the center coordinated by a N_4O_2 unit from two tridentate ligands that are almost perpendicular to each other (Fig. 1b, c and Fig. S1). Owing to the intermolecular O–H…N hydrogen bonds (Fig. 1d, Fig. S1) and π–π stacking interactions between the conjugated ligands, the individual asymmetric units link into a three-dimensional supramolecular network structure. Temperature-dependent magnetic susceptibility measurements verify the SCO nature of **1**, switching between LS and HS states (Fig. 1e). The transition temperature is ~295 K/ ~ 285 K during heating/cooling with a hysteresis of ~10 K, showing typical character of the first-order transition.

Barocaloric performance of 1

The thermal effect under hydrostatic pressure with N_2 being pressure transmitting medium was measured by pressure differential scanning calorimetry (P-DSC) with a temperature ramping rate of 0.5 K/min (Fig. 2a). The transition temperatures during heating and cooling at ambient pressure, defined as the peak positions in the P-DSC curves, were 297 K and 280 K, respectively, which were slightly different from the values obtained from the SQUID measurements (~295 K/ ~ 285 K) owing to the different sample environments. The corresponding entropy changes for both heating and cooling were calculated to be ~87 $J{\cdot}K^{-1}{\cdot}kg^{-1}$ at ambient pressure (this value is slightly larger compared with the original literature[53], which is likely attributed to the different DSC devices used. See the Methods for details). However, an interesting phenomenon occurred when pressure was applied: the entropy change ΔS gradually increased from 87 $J{\cdot}K^{-1}{\cdot}kg^{-1}$ at 0 MPa to ~125 $J{\cdot}K^{-1}{\cdot}kg^{-1}$ and reached saturation above 7.5 MPa (Figs. S2, 3). Moreover, the transition temperature (T_c) showed quasi-unreasonable pressure sensitivity (Fig. 2b). The dT_c/dP reached ~5.56 K/MPa at low pressure ($P < 5$ MPa) and 0.957 K/MPa when $P > 20$ MPa, which is the

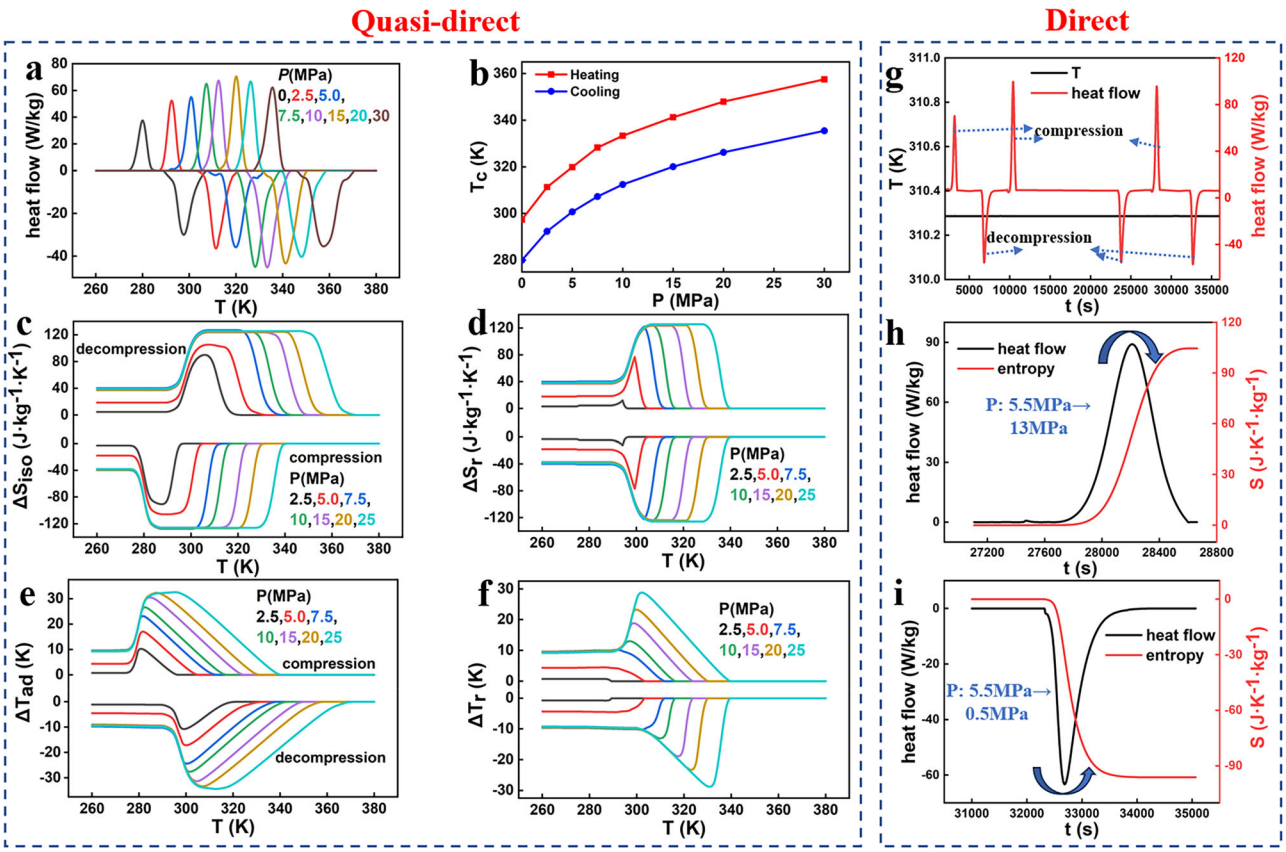


Fig. 2 | Barocaloric performance of 1 determined by pressure differential scanning calorimetry (P-DSC) via quasi-direct and direct methods. a Heat flow curves of **1** under various pressures with a temperature scanning rate of 0.5 K/min. **b** Change of the transition temperature (T_c) of **1** with the applied pressure. **c** Isothermal entropy change (ΔS_{iso}) of **1** at various pressures obtained from the pressure–variable entropy change curves (Fig. S2). **d** Reversible entropy change (ΔS_r) of **1** obtained by overlapping the compression and depressurization from **c**. **e** Adiabatic temperature change (ΔT_{ad}) of **1** obtained from the pressure-dependent entropy curves including the contribution of the specific heat (Fig. S5). **f** Reversible adiabatic temperature changes (ΔT_r) of **1** determined from the heating entropy curve at atmospheric pressure and the cooling curves under external pressure. **g** Heat flow measured upon cyclic compression and decompression at a constant temperature of 310.7 K by P-DSC omitting noise (This microcalorimeter allows isothermal measurement of the thermal signal during the pressurization/depressurization process; see details provided in Note S1). The directly measured heat flow and ΔS_{iso} during the **h** pressurization and **i** depressurization cycle.

Table 1 | Barocaloric performance of $Fe(PC4HH)_2$ compared with representative organic and inorganic BCE materials

	compound	ΔS_r 7.5 MPa ($J \cdot kg^{-1} \cdot K^{-1}$)	ΔT_r 30 MPa (K)	dT_c/dP (K/MPa)	RC_{rev} 30 MPa ($J \cdot kg^{-1}$)	RC_{rev}/P 30 MPa ($J \cdot kg^{-1} \cdot MPa^{-1}$)	Ref.
organic	$C_{16}H_{34}$	100	<8	0.25	2600	86.66	28
	$C_{18}H_{38}$	120	<5	0.2	2060	68.53	28
	Para-carborane	<5	<5	0.38	200	6.67	67
	NPG	0	0	0.13	0	0	25,26
	PG	0	0	0.094	0	0	29
	NPA	0	0	0.22	0	0	29
	TRIS	0	0	0.037	0	0	29
	AMP	0	0	0.085	0	0	29
	PEG10000/PET15000	0	0	0.097	0	0	22
	$(C_9H_{19}NH_3)_2MnCl_4$	<5	1	0.172	190	6.43	23
	$(C_{10}H_{21}NH_3)_2MnCl_4$	<10	1	0.18	640	21.43	23
	$(NA)_2CuBr_4$[a]	40	10	35	460	920	54
inorganic	$Fe[HB(tz)_3]_2$	75	<5	0.22	360	12	42
	$Fe(L)(NCS)_2$	20	5	0.194	750	25	51
	$Fe_3(bntrz)_6(tcnset)_6$	20	6	0.25	500	16.67	52
	[TPrA][Mn(dca)$_3$]	30	<10	0.231	235	7.84	68
	$C_7H_{14}NReO_4$	0	0	0.138	0	0	69
	$[Cp_2Fe][PF_6]$	10	3	0.341	130	4.38	70
	$MnCoGeB_{0.03}$	0	0	-0.1	0	0	71
	AgI	0	0	0.24	0	0	57
	$(NH_4)_2SO_4$	0	0	0.045	0	0	72
	C_{60}	<8	<8	0.172	180	6	73
	NH_4I	0	<12	0.79	150	5	74
	$Fe(PC4HH)_2$	125	30	5.56 (P < 5 MPa) 0.957 (P > 20 MPa)	4884	162.8	**This work**

[a]The data for $(NA)_2CuBr_4$ are all obtained under 0.5 MPa in C_3H_8 atmosphere.
Reversible entropy change (ΔS_r) and adiabatic temperature change (ΔT_r), pressure sensitivity (dT_c/dP), reversible refrigeration capacity (RC_{rev}), and RC_{rev}/P are given.

record-high ones among reported BCE materials (Table 1), except $(NA)_2CuBr_4$ in C_3H_8[54]. Such a value deviates largely from the calculated 0.22 K/MPa ($P < 5$ MPa) and 0.70 K/MPa ($P > 20$ MPa) from the Clausius-Clapeyron relation and lattice parameters (*vide infra* in the PXRD section). This kind of anomaly has occurred before[55], but the deviation was much smaller than in **1**. Based on the series curves, the isothermal barocaloric entropy change ΔS_{iso} and its counterpart, the adiabatic temperature change ΔT_{ad}, considering the specific heat (C_p) contribution, were quasi-directly determined (Fig. 2c and e)[21–24]. The maximum value of ΔS_{iso} was ~125 $J \cdot K^{-1} \cdot kg^{-1}$ at a low pressure of 7.5 MPa, and the upper limit for ΔT_{ad} was ~30 K at 30 MPa.

Considering practical merit, the reversible entropy change ΔS_r and reversible adiabatic temperature change ΔT_r are more attractive after subtracting the hysteresis (Fig. 2d, f). The value of ΔS_r reached a peak of ~125 $J \cdot K^{-1} \cdot kg^{-1}$ at a small pressure of ~7.5 MPa, and the temperature span was ~40 K under 30 MPa, which results in a large reversible refrigeration capacity (RC_{rev}) of ~4884 J/kg (the maximum ΔS_r multiplied by the peak width at half height, Fig. 3, Fig. S3b), which can only be achieved under pressure more than 200 MPa for most other BCE materials[25,26,42,52,56,57]. The reversible ΔT_r reached ~30 K at ~30 MPa and ~302 K (near room temperature). **1** shows outstanding BCE properties under low pressure compared with representative inorganic and organic BCE materials (Fig. 3, Table 1). Note that the RC_{rev} ~ 4884 J/kg was nearly four times higher than the highest reported value in the literature (*n*-alkanes, ~1100 J/kg). Furthermore, in terms of the coefficient of refrigerant performance ($CRP = |\Delta T_r \Delta S_r / W|$)[42], which describes the efficiency of caloric materials for converting the input work W into reversible thermal changes (approximated by $\Delta T_r \Delta S_r$), sample **1** (CRP > 5) stands out among reported BCE materials (Fig. S34a).

To verify the colossal BCE driven by low pressure, we further performed direct measurements of isothermal entropy change at a constant temperature of 310.7 K (Note S1, Fig. S9–S12, Table S8). The phase transition repeatedly occurred with three successive cycles of pressurization and depressurization, which is indicated by the conspicuous exothermic peaks from ~5.5 to ~13 MPa (Fig. 2h and Fig. S7) and endothermic peaks from ~5.5 to ~0.55 MPa (Fig. 2i and Fig. S8). The corresponding reversible isothermal entropy change was ~100 $J \cdot K^{-1} \cdot kg^{-1}$, which was in line with the entropy change determined by the quasi-direct method around 310 K considering the different pressure mode (Fig. 2d).

Variable-temperature/pressure powder XRD (VT/VP-PXRD)

To understand the large dT_c/dP and large BCE driven by low pressure, we first performed variable-temperature powder XRD (VT-PXRD) to investigate the structural changes during phase transition. The structure of the HS state was previously determined by single-crystal XRD[48], but the LS phase is unknown. In comparison of LS with HS phase (Fig. S14a, b), the peaks at 16°, 18°, 26°, and 27° in the PXRD patterns all disappeared after the transformation from the HS to the LS phase, and three new peaks appeared at 15.3°, 19.5°, and 26.7°. The first two peaks in the low-angle range (8.5° and 9.7°, i.e., the (200) and (110) peaks, respectively) were nearly identical for both spin states, indicating that the difference between the lattices was not large. We successfully refined the PXRD spectra at various temperatures by Le Bail method (Fig. 4d, f and Fig. S16–S28). The space group of the LS phase was the same as that of the HS phase (*C*2/*c*). The main differences in the transition from the HS to LS states occurred in the lattice parameters. The *a* parameter decreased, the *b* parameter was nearly unchanged, the *c* parameter increased, and the β angle decreased from the HS to

https://doi.org/10.1038/s41467-026-77679-7

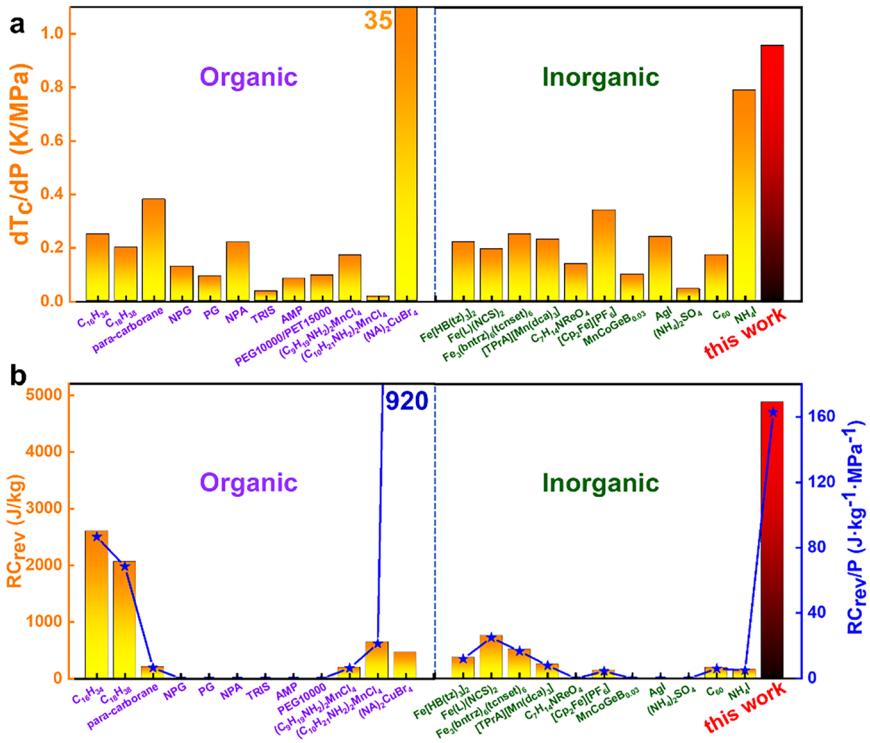


Fig. 3 | Barocaloric performance of $Fe(PC4HH)_2$ compared with representative organic and inorganic BCE materials. a Pressure sensitivity of phase transition temperature dT_c/dP. **b** Reversible refrigeration capacity RC_{rev} under 30 MPa (left axis, histogram) and the corresponding reduced RC_{rev}/P by pressure of 30 MPa (right axis, point plot). The dT_c/dP and RC_{rev}/P for $(NA)_2CuBr_4$ are 35 K/MPa and 920 J·kg^{-1}·MPa^{-1} respectively and the numbers have been marked in the figures. Note that this value can only be obtained with the pressure transmitting medium being C_3H_8. Materials include n-alkanes $C_{16}H_{34}$ and $C_{18}H_{38}$[28], carboranes para-carborane[67], organic plastic crystals PG, NPG, NPA, TRIS, and AMP[25,26,29], the macromolecular substance PEG10000[22], organic-inorganic hybrid materials $(C_9H_{19}NH_2)_2MnCl_4$, $(C_{10}H_{21}NH_2)_2MnCl_4$[23], and $(NA)_2CuBr_4$[54], spin-crossover materials $Fe[HB(tz)_3]_2$[42], $Fe(L)(NCS)_2$[51] and $Fe_3(bntrz)_6(tcnset)_6$[52], hybrid perovskite $[TPrA][Mn(dca)3]$[68], ferroelectric plastic crystals $C_7H_{14}NReO_4$[69], molecular salts $[Cp_2Fe][PF_6]$[70], ferromagnetic $MnCoGeB_{0.03}$[71], superionic conductor AgI[57], ammonium sulfate $(NH_4)_2SO_4$[72], fullerite C_{60}[73] and inorganic NH_4I[74]. Details are also listed in Table 1.

the LS phase (Fig. S14c, d). The expansion of lattice volume from LS to HS phase was ~2.7% (Fig. S14e), which is not sufficiently large to support the significant dT_c/dP and the corresponding barocaloric ΔS_{iso}. Note that the estimated dT_c/dP of 0.22 K/MPa was much smaller than the measured values of ~5.56 K/MPa ($P < 5$ MPa) and ~0.957 K/MPa ($P > 20$ MPa) using $\Delta S = 87$ J·K^{-1}·kg^{-1} based on the Clausius–Clapeyron equation ($dT_c/dP = \Delta V/\Delta S$).

To explore the origin of high sensitivity of T_C to pressure for sample **1**, we then performed variable-pressure powder XRD (VP-PXRD) using a conventional diamond anvil cell (DAC) owing to the lack of a low-pressure (<30 MPa) device, and the results are shown in Fig. 4a, b, c, e. Because the sample was loaded into a DAC, the signal-to-noise ratio was not as good as that of VT-PXRD. However, some remarkable changes were still observed. The spectrum before compression was clearly that of the HS phase, although the peak positions were different from those obtained by VT-PXRD owing to the different source used (i.e., Cu target for VT-PXRD and Mo target for VP-PXRD) (Fig. 4a). During compression, the peak at approximately 4.5° disappeared while a new peak appeared at ~5° and moved to higher angle with higher applied pressure. In addition, a remote new peak appeared at ~19.7° from 0.36 GPa (cycled in Fig. 4b), which was absent during VT-PXRD (Fig. 4b). Such changes in the PXRD spectrum indicate that a new LS phase may be induced by external pressure. The lattice at 1.48 GPa was obtained following Le Bail refinement (Fig. 4e and Table S4), and the corresponding parameters were indicated by solid balls in Fig. S1c–e. Compared with the initial LS phase (LS-1), the a parameter greatly increased, the b parameter decreased, the c parameter changed little, and the β angle increased from 102.7° in LS-1 to ~108°. These changes caused the lattice volume to decrease from ~2548 Å^3 for the HS phase to ~2260 Å^3 for the possible new phase (LS-2), with $\Delta V/V$ ~ 13% (Fig. S14e). This volume change seems to be sufficiently large to support the large dT_c/dP and the increase of ΔS (Fig. S3a). Note that the dT_c/dP value of ~0.7 K/MPa approached the measured value of ~0.95 K/MPa using ΔS ~ 125 J·K^{-1}·kg^{-1} based on $dT_c/dP = \Delta V/\Delta S$.

Variable temperature/variable pressure (VT/VP) Raman spectroscopy

To verify the structural transition in sample **1**, especially the pressure-induced LS-2 phase, we further performed VT/VP Raman measurements also using a DAC, and the results are shown in Fig. 5. Upon heating, the spectrum changed at approximately 270 K (transition temperature), which was ~20 K lower than that observed in other measurements owing to the thermal effect caused by the laser beam. When the temperature was below 263 K, the peak at 1366 cm^{-1} ascribed to ν(C–O) and the two peaks at ~1600 cm^{-1} attributed to ν(C = N–N = C) of hydrazone were unremarkable for LS-1[53]. After heating to above 273 K, the ν(C–O) band became the most intense in the whole spectrum, and the pair of peaks for ν(C = N–N = C) also greatly increased compared with the nearly zero intensity of the peaks for LS-1. Furthermore, the small peak at ~590 cm^{-1} disappeared with the transition from LS-1 to HS. For the VP measurements, when the sample was loaded into the DAC without applied pressure, its spectrum was the typical one of HS phase characterized by an intense peak at 1366 cm^{-1} and a doublet at ~1600 cm^{-1}. Upon compression to ~0.27 GPa, the spectrum was nearly the same as that of LS-1 with a characteristic small peak at ~590 cm^{-1} and weak ν(C–O) and ν(C = N–N = C) bands. When the pressure was further increased, a series of new spectra different from those of both LS-1 and the HS phase appeared from 0.41 GPa, as

https://doi.org/10.1038/s41467-026-77679-7

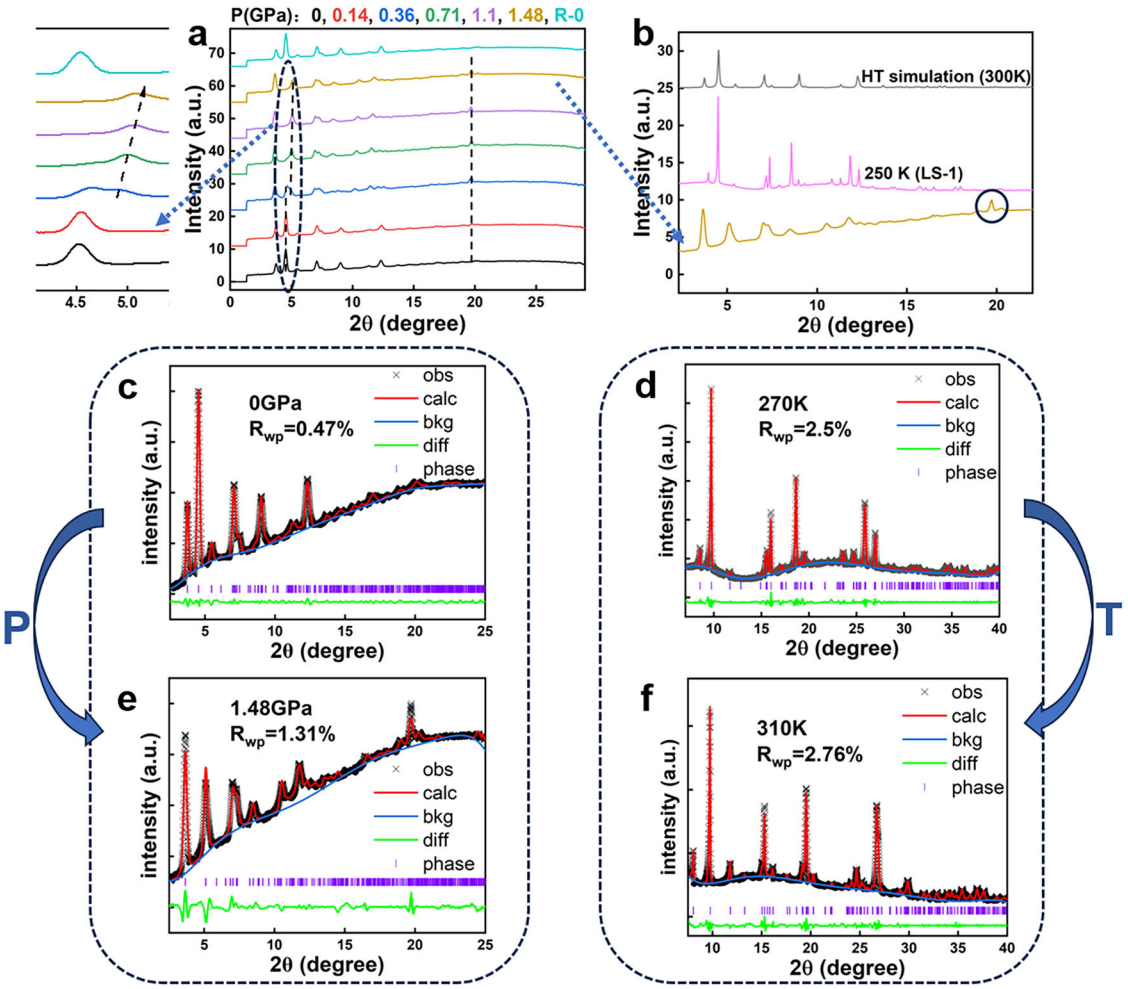


Fig. 4 | Structural changes of 1 induced by temperature and applied pressure. **a** X-ray diffraction spectra of **1** under various pressures. An enlargement of the change of the position of the peak at ~5° is shown at the left of **a**, where the change is indicated by the arrow. **b** Comparison between the spectrum under 1.48 GPa and the spectra of LS-1 (250 K) and the HS phase (300 K). Le Bail refinement results of **c** atmospheric pressure in the DAC and **e** under 1.48 GPa. Le Bail refinement results of **d** 270 K and **f** 310 K at atmospheric pressure.

shown in Fig. 5b. The single peak located at ~1010 cm^{-1} under atmospheric pressure (HS phase) and missing at 0.27 GPa (LS-1) split into a pair of peaks for the new phase (LS-2) from 0.41 GPa. In addition, the wavenumber of ν(C−O) gradually blue-shifted with applied pressure, and the two peaks of the ν(C = N−N = C) band merged into a single peak with a larger peak width above 0.41 GPa. However, they all returned to the original position in the spectrum of the initial HS phase after pressure relief. Together, these phenomena confirmed the existence of the pressure-induced LS-2 phase (see details given in Note S4). Moreover, considering the dT_c/dP~0.22 K/MPa from VT-PXRD (Fig. S14), the results of VP-Raman spectra from 0 GPa (HS) to 0.11 GPa (HS) to 0.27 GPa (LS-1), i.e., the process of HS to LS-l transition driven by pressure (Fig. 5b), conform to the Clausius−Clapeyron equation. However, the practical *P-T* diagram measured from P-DSC with N_2 being pressure transmitting medium (Fig. S13) seriously conflicts with the theoretical dT_c/dP~0.22 K/MPa from Clausius−Clapeyron equation.

Synchrotron radiation PXRD (SR-PXRD) under low pressure (<30 MPa)

Although some results were obtained via VT/VP-PXRD/Raman experiments with DAC, there were unresolved discrepancies in the relevant data. The main problem is that, due to the lack of low-pressure device, the applied pressure by DAC (0.11 ~ 1.48 GPa, pressure error is usually 50 MPa[58]) during our first-round VT/VP-PXRD/Raman experiments are much larger than the one used in our P-DSC measurements (<30 MPa). In order to solve this problem, we constructed a VT/VP device (250−330 K, resolution: 0.01 K; 0~30 MPa resolution: 0.01 MPa) equipped on synchrotron radiation PXRD via gas being the pressure-transmitting medium. Then VP/VT-PXRD measurements were conducted in SSRF (Shanghai Synchronous Radiation Facilities) to reveal the mechanism behind the amazing BCE of sample **1**. Unsurprisingly, we did not detect the emergence of the new LS-2, but indeed detected the SCO transition between HS and origin LS-1 under a small pressure <20 MPa.

As shown in Fig. 6a, the diffraction spectra at 260 K under ambient pressure were typically in the LS-1 phase and remained unchanged in the compression process up to 20 MPa, inferring that **1** is always in the LS-1 phase at 260 K. The same situation was observed at 290 K on heating, where **1** was also in the LS-1 state all the while during the VP procedure (Fig. 6b). The corresponding cell parameters at variable pressure at 260 K and 290 K were obtained via Le bail refinement and the results were illustrated in Fig. 7a, b, respectively. One can see that the *a* axis decreased while *b* and *c* axis increased slightly with increasing pressure for both temperatures, and no strange phenomenon was found here.

With further increasing temperature to 310 K, the diffraction spectrum became the HS phase under 0 MPa, which then converted

https://doi.org/10.1038/s41467-026-77679-7

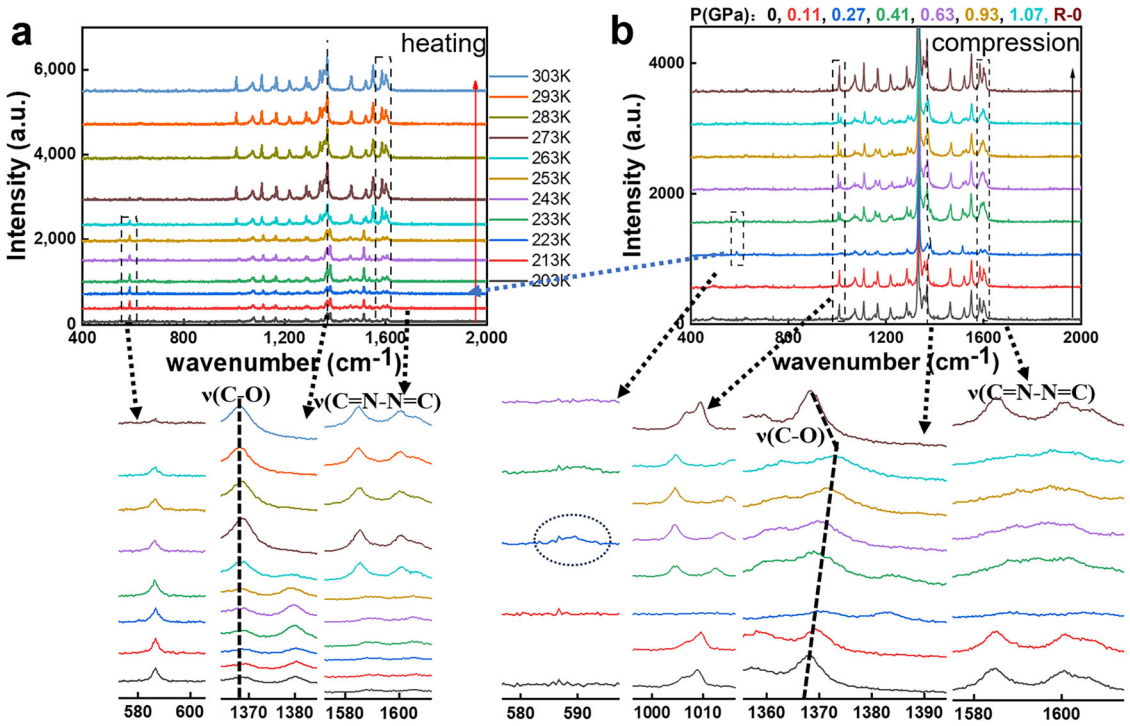


Fig. 5 | Variable-temperature/pressure Raman spectroscopy. a Variable-temperature Raman spectra of **1** during heating. **b** Variable-pressure Raman spectra of **1** at 298 K. The changes of the corresponding peaks are indicated by dashed lines and rectangles, and enlarged views of certain bands are shown below **a** and **b**. The blue dotted arrow indicates that the spectrum of **1** at 0.27 GPa is nearly the same as the those below 263 K under ambient pressure.

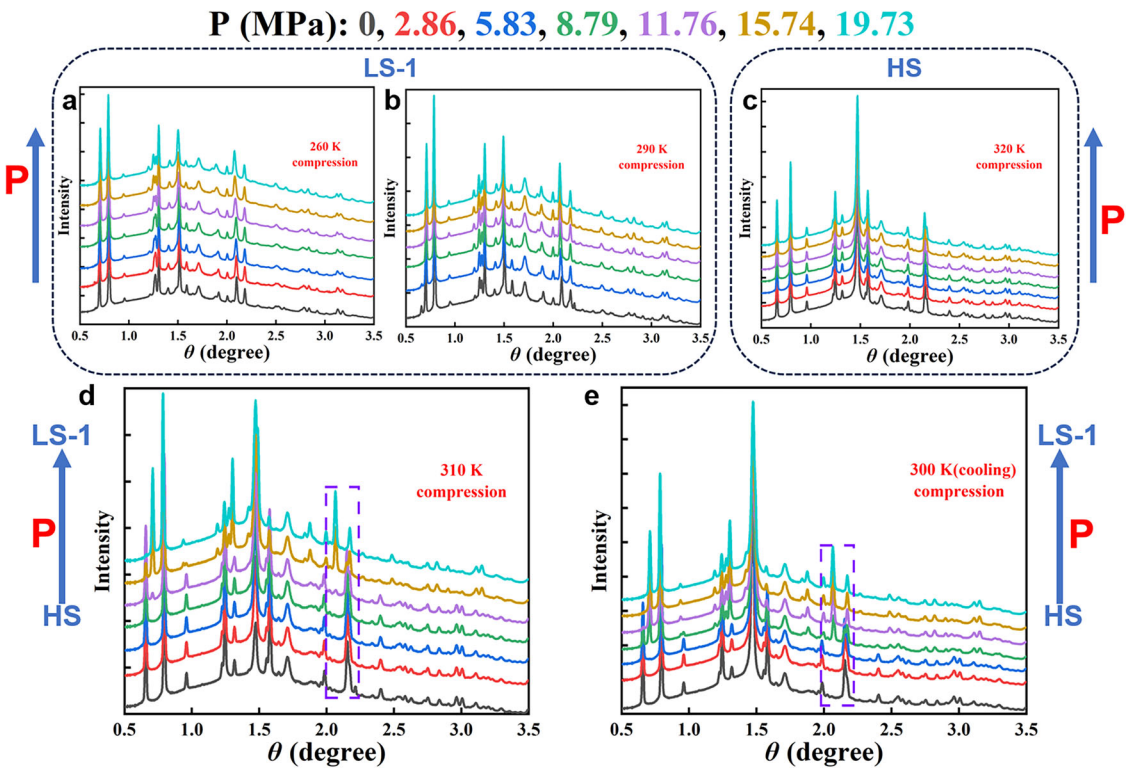


Fig. 6 | VT/VP-SR-PXRD with gas being pressure transmitting medium. a VP-PXRD at 260 K from 0 MPa to 20 MPa. **b** VP-PXRD at 290 K from 0 MPa to 20 MPa. **c** VP-PXRD at 320 K from 0 MPa to 20 MPa. **d** VP-PXRD at 310 K from 0 MPa to 20 MPa. **e** VP-PXRD at 300 K in cooling process from 0 MPa to 20 MPa. The most remarkable change of diffraction peaks from HS to LS-1 have been circled by the purple rectangles in (**d**) and (**e**).

https://doi.org/10.1038/s41467-026-77679-7

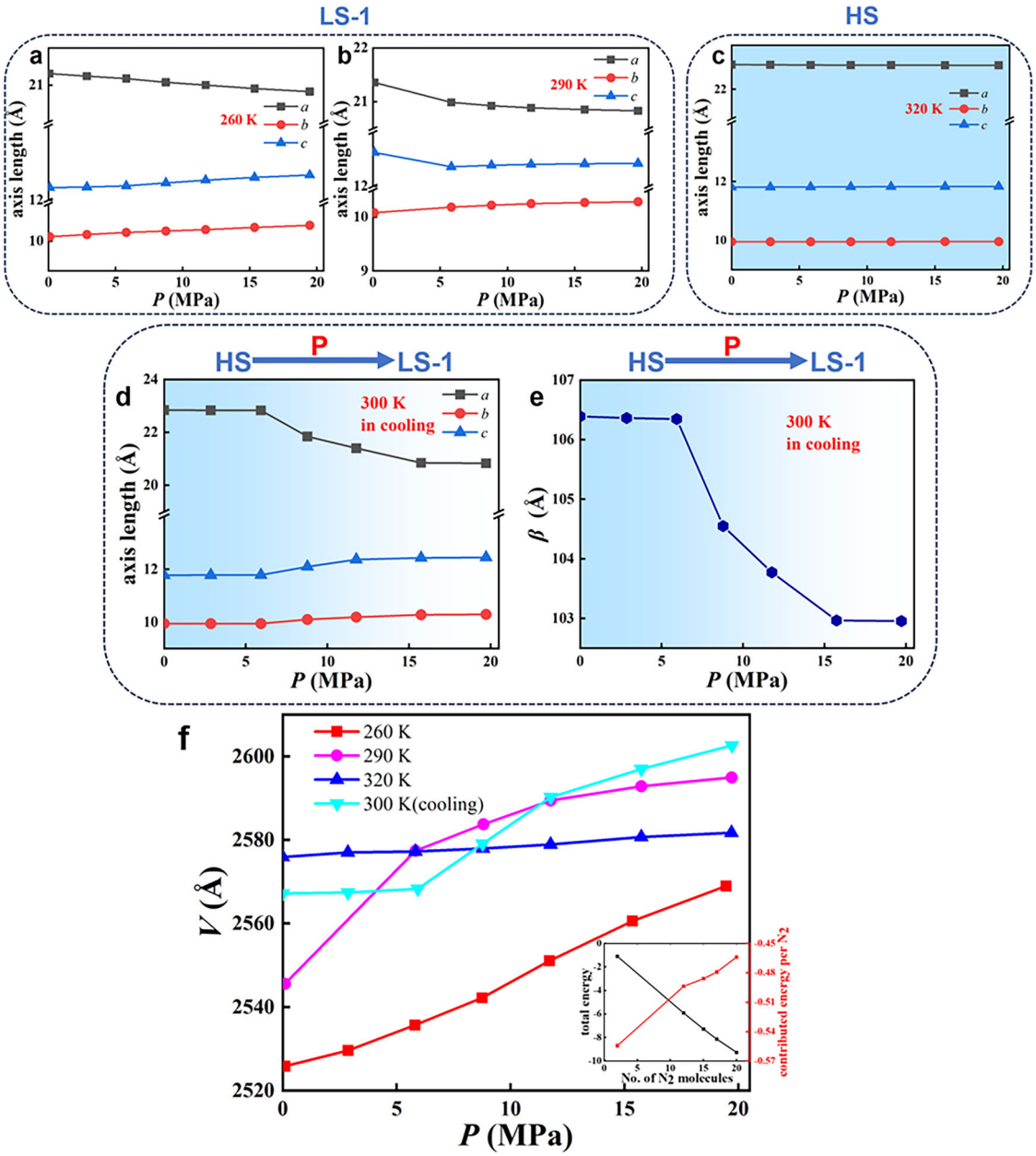


Fig. 7 | Lattice parameters from VP-SR-PXRD with gas (air) being pressure transmitting medium. The corresponding changes of cell parameters with applied pressure from 0 to 20 MPa at **a** 260 K, **b** 290 K and **c** 320 K in heating. **d** The evolution tendency of cell axes *a*, *b* and *c* with pressure from 0 to 20 MPa at 300 K in cooling. **e** Trend of *β* angle with pressure from 0 to 20 MPa at 300 K in cooling. **f** The evolution tendency of lattice volume with pressure at various temperatures. Inset: The total energy of LS-1 with N_2 (left axis) and the contributed energy per N_2 molecule (right axis).

into the original LS-1 under compression at around 11.76~15.74 MPa (Fig. 6d). This phenomenon solidly confirmed that the SCO phase transition can be driven under this small pressure, and the value of this pressure exactly falls on the *T-P* diagram obtained from P-DSC with N_2 being pressure transmitting medium (Fig. S13) considering that the pressurization process corresponds to the cooling process due to hysteresis[42,59]. As for the spectra obtained at 320 K (Fig. 6c), the diffraction spectra were all in the HS phase at all pressures, i.e., the SCO phase transition from HS to LS-1 cannot be driven up to 20 MPa at 320 K, also basically corresponds with the *T-P* diagram (Fig. S13). Upon cooling and when the sample reached 300 K, it should be still in the HS phase due to thermal hysteresis as per the *T-P* diagram under ambient pressure. Not surprisingly, the measured spectrum at 300 K (Fig. 6e) in cooling under ambient pressure is indeed still in the HS, but upon pressurization, the SCO phase transition from HS to LS-1 can be driven by a pressure as small as 5.83–8.79 MPa, and this value also falls on the *T-P* diagram obtained from P-DSC (Fig. S13). The critical pressure at 300 K is lower than the critical 11.76–15.74 MPa driving SCO phase transition at 310 K (Fig. 6d), because 300 K was closer to the T_c under 0 MPa (for cooling, T_c~280 K).

Figure 7d, e show the cell parameters with pressure at 300 K, a temperature point involving both LS-1 and HS phase. One can see there is a conspicuous change in the three cell axes and the *β* angle under pressurization. Specifically, the *a* axis decreased from ~23 Å to ~21 Å after entering the LS-1 phase, while *b* axis increased from 9.97 Å to 10.07 Å from HS to LS-1 transition, and *c* axis was nearly unchanged. Meanwhile, the *β* angle is 106.5° in the HS phase, which also decreased to the typical value of 102.8° of the LS-1 phase according to the data from VT-PXRD (Fig. S14). This result again verified that the SCO transition can be driven under a small pressure of around 5.8–8.8 MPa,

conforming well to the conclusion obtained from the above P-DSC with N_2 being the pressure-transmitting medium (the maximal ΔS_r was quasi-directly obtained at ~7.5 MPa, falling in this pressure range). In contrast, there was little change in the cell parameters with pressure at 320 K of HS phase (Fig. 7c) compared with the situation at 260 K and 290 K of LS-1 phase (Fig. 7a and b), indicating that the influence of pressure on the HS phase is less than that on LS-1 phase.

The corresponding cell volumes under various temperatures and pressures were summarized in Fig. 7f. What is out of our expectation is that, no matter whether it is in LS-1 or HS, the lattice volumes all increased with applied pressure instead of shrinking. It is so strange since materials' volume generally would decrease under compression, but here the inverse trend was observed in **1**. Considering the pressure-transmitting medium is gas (air) in our small-pressure device equipped on SR-PXRD, the only reason for this singular result is that the gas molecules enter the sample under pressure and therefore expand the lattice. Specifically, the trend of *V-P* shown in Fig. 7f is also different for different temperatures.

At 260 K of LS-1 phase, the *V-P* relationship is nearly a straight line without remarkable traits, while at 290 K closer to the SCO transition T_c ~ 297 K (upon heating, ambient pressure), the *V-P* relationship shows an interesting tendency: at low pressure range (0 ~ 5 MPa), the increment of *V* was fast, while in the high pressure range (10 ~ 20 MPa), this increment tended to become slower and slower, i.e., a saturation trend appears with progressively higher pressure. However, the *V-P* relation at 320 K of HS phase behaves quite differently (the sample retains HS up to 20 MPa, see Fig. 6c). The volume increases little and remains nearly unchanged with pressure even up to 20 MPa at 320 K (Fig. 7c), indicating that in the HS phase it is difficult for gas molecules to adsorb into the lattice of **1**. Further, the results at 300 K again confirmed the *V-P* trend for both LS-1 and HS (Fig. 7f). At 300 K (in cooling), **1** was initially in the HS phase (Fig. 6e), and in the low pressure range below 5 MPa, the cell volume changed little with pressure (Fig. 7f); however, when the HS to LS-1 transition was completely driven by pressure above 8.79 MPa (Fig. 6e), the *V-P* relation becomes very similar with the LS-1 phase observed at 290 K (Fig. 7f), also having a saturation trend with pressure. This specific result further confirmed that the gas adsorption probability in LS-1 and HS phase is different: the LS-1 phase is more favorable with external gas compared with the HS phase. Here, it is noteworthy that the unit-cell volume (Fig. 7f) refined from SR-PXRD patterns represents only the crystallographic volume of the gas-absorbed solid, while the signals of the single gas (N_2) acting as the pressure medium cannot be simultaneously detected. Gas adsorption enlarges the lattice of solid, probably through steric effects, guest–framework interactions, and relaxation of the flexible framework[60,61], but does not imply a negative compressibility of the entire solid–gas system due to the compressible gas. Similar pressure-induced lattice expansion by gas adsorption was also observed in metal–organic frameworks (MOFs)[60,61], where the uptake of gas molecules leads to an increase in the unit-cell volume with increasing external pressure.

Moreover, the discrimination of gas adsorption for LS-1 and HS was illustrated by DFT calculations as listed in Table S5. The initial lattice volumes after optimization for LS-1 and HS were 2655.00 $Å^3$ and 2747.96 $Å^3$, respectively, based on the structural information from Rietveld refinement of VT-PXRD and the.cif file from previous literature[53]. After the insertion of 20 N_2 molecules (N_2 accounts for ~78% of air) to simulate gas adsorption, the volume for LS-1 and HS changed to similar values of 2869.23 $Å^3$ and 2870.90 $Å^3$, respectively. Because the initial volume of LS-1 was conspicuously smaller than that of HS, the expansion trend after the entry of N_2 molecules into the LS-1 was more significant than HS, congruent with the results observed in Fig. 7f.

Based on above analysis, it can be inferred that the entropy change across SCO phase transition under pressure would be from two sources (take heating as example), i.e., one is the intrinsic SCO transition with entropy change ~87 $J{\cdot}K^{-1}{\cdot}kg^{-1}$ (Fig. S2), while the other is the entropy change caused by the desorption of gas molecules adsorbed in the lattice of LS-1 under pressure, because HS is quite unfavorable for gas adsorption compared with LS-1 as discussed above. Hence after the spin state of the central Fe(II) ion transfers from LS-1 to HS, the gas molecules would immediately desorb from the lattice, which would also absorb heat; that is, this process also contributes an amount of entropy change. Therefore, the total entropy change would be $(87+x)$ $J{\cdot}K^{-1}{\cdot}kg^{-1}$, where x is the entropy change contributed by gas desorption and finally the measured entropy change by P-DSC (also the total entropy change) would increase with pressure (Fig. S2a). In addition, as illustrated in Fig. 7f, the cell volume at 290 K (close to T_c under 0 MPa) rises gradually with pressure and shows a saturation trend, which means the amount of gas molecules adsorbed in the lattice at LS-1 would also show a similar trend with saturation effect. Since the entropy change from gas desorption x is proportional to the amount of gas existing in the LS-1, it can be reasonably concluded that the x would also be a function with saturation phenomenon under pressure, and finally the total entropy change $(87+x)$ $J{\cdot}K^{-1}{\cdot}kg^{-1}$ was born with such an effect as presented in Fig. S2.

Besides the anomalous increase of entropy change, the ultra-sensitive T_c with pressure may also be explained in parallel. As the sample was at the LS-1 phase, particularly around T_c, it is reasonable to say that the higher the pressure is, the more gas molecules would adsorb into the lattice, and meanwhile the binding effect between gas molecules and lattice would become stronger with increasing pressure. Thus, a higher temperature would be required to eliminate these gas molecules to complete the total SCO phase transition since the gas desorption and the transfer of the spin state of central Fe(II) is coupled together; consequently, the T_c would shift faster to higher temperatures under pressure. DFT calculations support this result (Inset of Fig. 7f). With inserting N_2 (account for 78% of air) into LS-1 lattice, the total energy gradually decreases (left axis of inset in Fig. 7f), while the contributed energy per N_2 molecule increases with increasing the number of N_2 molecules, indicating that LS-1 phase with more N_2 shows more stable trend and a higher temperature would be required to make the N_2 desorption. The gradually increased energy contributed per N_2 implies that a saturation trend may appear for LS-1 with more N_2 (right axis of inset in Fig. 7f). Moreover, resembling the trend of cell volume at 290 K (close to T_c under 0 MPa), it rises fast under low pressure (<5 MPa) and shows a saturation effect (rising slowly under pressure >10 MPa), the amount of gas molecules adsorbed into the lattice would also show this trend with pressure, and finally the T_c-P relation would also conform to such a regularity as presented in Fig. 2b, i.e., T_c increase fast when $P < 5$ MPa, and the higher the pressure, the increase speed of T_c would be slower.

Discussion

The colossal and ultra-sensitive pressure response for the SCO T_c originates from the gas complexation with the sample **1**, which was revealed by P-DSC and VP-SR-PXRD with gas (air) being the pressure-transmitting medium. From the initially measured VT-PXRD and lattice parameters (Fig. S14), the pressure sensitivity of T_c using Clausius–Clapeyron equation ($dT_c/dP = \Delta V/\Delta S$) was calculated as 0.22 K/MPa, which is much smaller than the measured value from P-DSC. However, it is consistent with VP-Raman results (T_c between HS and LS-1 at $P < 0.27$ GPa, Fig. 5b) measured by a DAC with silicon oil as the pressure medium. Note that the temperature of the detected Raman area of **1** is practically around ~320 K (~ 20 K higher than room temperature 300 K due to thermal effect of the laser as illustrated in Fig. 5a). As 0.11 GPa pressure was applied, the actual T_c (280 K) in cooling would shift to 304 K according to dT_c/dP ~ 0.22 K/MPa, still below the sample practical temperature 320 K, so the sample is still in the HS (Fig. 5b). When the pressure increased to 0.27 GPa, the T_c would

rise to 339 K (above 320 K), **1** transferred from HS to LS-1 (Fig. 5b). This means that under the DAC environment, the pressure was solely the compression effect on the sample, while the pressure medium of silicon oil cannot enter the lattice of **1** due to large size of oil molecules, so the dT_c/dP conforms to Clausius–Clapeyron equation.

The gas molecules during P-DSC (N_2) and SR-PXRD (air, 78% N_2) measurements not only transmit pressure, but also penetrate into the sample because of the small-sized gas molecules. Hence, the Clausius–Clapeyron equation that only works for pure single BCE material, is invalid for evaluating BCE performance of sample **1**. Furthermore, the penetration of gas molecules behaves quite differently with LS-1, much more favorable than that of HS, as shown in Fig. 7f. Such a phenomenon finally brought forth the singular BCE properties in **1**, including the saturation trend of entropy change under pressure and the ultra-high pressure sensitivity of T_c.

From the perspective of sample **1**, it is reasonable to say that the amazing BCE is the combination of the sample itself with the pressure-transmitting medium gas. It is due to the specific structure character of the sample that the external gas can then complex with the sample. This result infers that the structure of SCO complex itself is a key factor influencing the final BCE parameters. By designing various structures in the SCO complexes, it is likely that different BCE with influence from other media, possibly small molecules such as gas, H_2O and methanal, etc. can be obtained, and more interesting and considerable BCE performances can be expected.

In conclusion, the SCO complex **1** has been confirmed to have potential for sustainable BCE refrigeration. An entropy change as much as ~125 $J{\cdot}K^{-1}{\cdot}kg^{-1}$ can be reversibly driven by a practical pressure as small as ~7.5 MPa, while the reversible ΔT_r can be up to ~30 K under ~30 MPa, owing to the extremely high pressure sensitivity (dT_c/dP) of the SCO transition. In-situ VT/VP-PXRD and VT/VP-Raman via DAC demonstrated that a new LS phase (LS-2) develops by pure pressure ~0.4 GPa. With gas being pressure medium, in-situ SR-PXRD that can work under low-pressure range (<30 MPa) amazingly proved that the gas (air) molecules not only act medium but also penetrate into the sample with disparate absorption for LS-1 and HS phase. Eventually, the unique BCE performances appear in **1**, including the colossal BCE driven by small pressure, the ultra-high pressure sensitivity of T_c, and the increase and saturation trend of barocaloric entropy change with pressure. Our work demonstrates that with the combination of a pressure-transmitting medium and a spin-crossover complex, singular BCE performance can be achieved, benefiting from the intrinsic structural character of SCO complex, and a more attractive BCE material with larger dT_c/dP can be expected by tailoring specific structures in SCO materials.

Methods

Sample preparations

Polycrystalline sample **1** was prepared according to the methods provided in previous literature[53]. An equimolar amount of solid NaOH (8.0 mg, 0.2 mmol) was added to a suspension of ligand LH (L = 2-Pyridinecarbaldehyde-4'-hydroxybenzoyl hydrazone, 48.2 mg, 0.2 mmol) in MeOH. The deprotonated ligand solution was obtained after stirring and then methanol solution of iron(II) perchlorate (27.2 mg, 0.1 mmol) was added. The reaction mixture was stirred at room temperature for 1 h. The black-green powder was collected by filtration. After washing with cold MeOH (3×5 mL), **1** was obtained after drying at 40°C under vacuum. Yield: 40.7 mg 76 %. Anal. Calcd for $C_{26}H_{20}N_6O_4Fe$: C, 58.23; H, 3.76; N, 15.67. Found: C 57.89; H, 3.45; N, 15.62 %.

Magnetic measurements

The variable-temperature magnetic susceptibility measurements were carried out for sample **1** (~ 10 mg) using a Quantum Design VSM-SQUID-Magnetometer at an external field of 1000 Oe in the heating and cooling mode within a temperature range from 2 to 340 K with a temperature scanning rate of 1 K/min. Gelatine capsules were used as sample containers for measurements. The M-T curve of the sample holder was first measured, and then the data with the sample in the sample holder was collected. To obtain the pure data from only the sample, the data of sample holder was subtracted. To verify the SCO nature of **1**, the temperature dependence of the magnetic susceptibility was measured by a superconducting quantum interference device (SQUID) under a magnetic field of 1000 Oe (Fig. 1e). The $\chi_m T$ value was only ~0.032 $cm^3{\cdot}K{\cdot}mol^{-1}$ below 290 K, indicating the LS state of the central Fe^{2+}. It reached ~3.5 $cm^3{\cdot}K{\cdot}mol^{-1}$ at approximately 300 K, which is typical of the HS state of the Fe^{2+} ion. In the cooling process, $\chi_m T$ retained the HS value until a temperature of ~290 K, and it then sharply decreased and returned to the original LS value at ~280 K, which confirmed the reversibility of the phase transition. The transition temperature, which is defined as the peak position of $d(\chi_m T)/dT$, was ~295 K during heating and ~285 K during cooling, with a hysteresis of ~10 K, showing the typical character of the first-order phase transition.

Variable temperature powder X-ray diffraction (VT-PXRD)

PXRD at variable temperatures was measured by Rigaku Smartlab using Cu K_α radiation. The lattice parameters of the high-temperature state (HS) and low-temperature state (LS-1) were obtained by Le bail method using the GSAS suite.

Variable Pressure powder X-Ray Diffraction (VP-PXRD) via DAC

PXRD measurements under variable pressure were carried out using graphite-monochromated Mo-Kα radiation (λ = 0.71073 Å) on Rigaku Synergy Custom FR-X Diffractometer equipped with a Hybrid Photon Counting (HPC) X-ray detector (HyPix-6000HE). The powder sample was loaded into a diamond anvil cell (DAC) for testing. The CrysAlis software package was used for data collection and initial data reduction. Le Bail refinement was performed using GSAS software to obtain the lattice parameters.

Synchrotron radiation powder X-Ray Diffraction (SR-PXRD) under small pressure

The photo of the scene of our homemade device equipped on SR-PXRD is illustrated in Fig. S15. The pressure (0–30 MPa, resolution: 0.01 MPa) was controlled by a syringe pump and was monitored by a pressure gage (the pressure transmitting medium is air), while the temperature (250–330 K, resolution: 0.01 K) was controlled and monitored by the temperature sensor in the sample cell through PID method with the help of the thermostatic water tank providing a base temperature. The sample was sealed in the sample cell with both sides sealed by a beryllium slice (1 mm) to guarantee the gas tightness of the cell.

This pressure-controlled SR-PXRD was performed in SSRF (Shanghai Synchronous Radiation Facility), beamline BL12SW. The energy of the X-ray in our experiment is 98.5 keV, with the corresponding wavelength being 0.1259 Å. The X-ray spot is a square with side length of 0.5 mm, and the distance between the sample and the detector is 2.75 m. In addition, the detector is Pilatus 3 X CdTe 2 M, whose pixel size is 100 μm*100 μm. The 2D collected data with diffraction rings was then integrated with the GSAS II software to obtain the 1D Intensity-degree diagram.

Pressure DSC and specific heat measurements

The measurement of heat flow was performed using a pressure differential scanning calorimeter (μDSC7 evo microcalorimeter from SETARAM, temperature range: -40 ~ 120°C, pressure range: 0 ~ 100 MPa, calorimetric accuracy 40 nW, pressure resolution 0.01 MPa, temperature resolution 0.01 K). The sample mass for measurements is around ~10 mg. The temperature ramping rate was set to be 0.5 K/min during the whole process of heat flow measurement for barocalorics. High-purity N_2 gas (99.999%) was exploited to apply hydrostatic pressure ranging from atmospheric pressure to 30 MPa.

The specific heat capacity was also measured by the same calorimeter, the corresponding measurement part of which has been calibrated and tested by Naphthalene (Standard for GC, ≥99.5%(GC)). The entropy change of **1** in the original literature is 66 $J{\cdot}K^{-1}{\cdot}kg^{-1}$, smaller than the value obtained here. The value in ref. 53 is likely less accurate compared with the one obtained here due to the DSC device used. The DSC device used in ref. 42. is Q100 differential scanning calorimeter, which is around 15 years ago, while ours is the μDSC7 evo microcalorimeter from SETARAM, the latest product around the world since 2020, with a measurement accuracy of 40 nW, and therefore, the 46 $J\,K^{-1}mol^{-1}$ (87 $J{\cdot}K^{-1}{\cdot}kg^{-1}$) would be the right entropy change value due to the more accurate DSC device.

Variable temperature Raman spectroscopy (VT-Raman)

Raman spectra were measured with the Horiba Jobin Yvon HR800 confocal spectrometer, using a 532 nm laser as the excitation source. The Raman signal was recorded by a Princeton Instruments CCD detector and collected in the frequency range of 100–2400 cm^{-1}. The Rayleigh scattering was removed using a holographic notch filter. In order to avoid laser damage to the powder sample or the formation of local heat at the laser focus that affects the true temperature of the sample, the intensity of excitation light is <1 mW and the penetration length for this sample is ~2 μm. The temperature control of the variable temperature process was performed by the temperature control platform LINKAM THMS600/TMS94. The temperature was stabilized for 5 min before each temperature point was measured to keep the temperature even and accurate.

Variable pressure Raman spectroscopy (VP-Raman) via DAC

Raman spectra at variable pressure were measured with the Horiba Jobin Yvon HR800 confocal spectrometer. The excitation source was a 532 nm laser. A diamond anvil cell (DAC) composed of low-fluorescence I-type diamond was adopted, and silicone oil was used as the pressure transmission medium.

Direct measurement of isothermal entropy change ΔS_r driven by pressure

Direct measurement of isothermal entropy change ΔS_r driven by pressure was performed by μDSC7 evo microcalorimeter from SETARAM. The quasi-isothermal condition was constructed by a temperature control device combined with the slow operation of pressurization and depressurization to minimize the perturbation caused by compression and decompression. At a constant temperature set controlled by the corresponding device, the sample loaded into the vessel was first placed at a certain temperature with ~30 min to be stable; then ΔS_r induced by pressurization can be measured. After the compression, no action was done until the signal was stable again after the influence of noise disappeared. Next, the depressurization process (the inverse process of pressurization) was performed, and similarly the heat flow signal of the endothermic peak was detected. Through several pressurization-depressurization cycles, the reversible isothermal entropy change (ΔS_r) at a certain temperature can be obtained.

Measurements of barocaloric entropy change and adiabatic temperature change

Based on the heat flow (Q) response of temperature at variable pressure, the phase transition entropy curves can be constructed via the integration of heat flow:

$$S_{pt}(T,P) = \int_{T_0}^{T} \frac{1}{T'} \frac{Q(T',P)}{\dot{T}'} dT' \tag{1}$$

Considering the thermal response besides the latent heat of phase transition, the total entropy curves can be constructed including the specific heat capacity contribution, where specific heat capacity C_P at variable pressures were approximated as that for atmospheric pressure[56]:

$$S(T,P) = S_{pt}(T,P) + \int_{T_0}^{T} \frac{C_p}{T'} dT' \tag{2}$$

Barocaloric isothermal entropy change curves (ΔS_{iso}) were obtained quasi-directly by isothermal subtraction of entropy curves at variable pressure: $\Delta S_{iso}(T, P_0 \to P_1) = S(T,P_1) - S(T,P_0)$. Specifically, the ΔS_{iso} for the pressurization process ($P_0 < P_1$) utilizes the $Q(T,P)$ on cooling, while the ΔS_{iso} for the depressurization ($P_0 > P_1$) process utilizes the $Q(T,P)$ on heating. And the reversible isothermal entropy change ΔS_r is the overlap of ΔS_{iso} between pressurization and depressurization processes.

Barocaloric adiabatic temperature change (ΔT_{ad}) was obtained quasi-directly by adiabatic subtraction of entropy curves at variable pressure: $\Delta T_{ad}(T, P_0 \to P_1) = T(S,P_1) - T(S,P_0)$. Similar to ΔS_{iso}, the ΔT_{ad} for the pressurization process should be decided by entropy curves on cooling, while the ΔT_{ad} for the depressurization process be determined by entropy curves on heating. The reversible adiabatic temperature change ΔT_r was obtained by the adiabatic subtraction of heating entropy curve at atmospheric pressure and the cooling entropy curve at the applied pressure[57].

The isothermal entropy change during the direct measurement was calculated by the equation:

$$\Delta S_{qit} = \frac{1}{T} \int_{t_0}^{t_1} \dot{Q} dt \tag{3}$$

where T is the environment temperature in the experiment, $\dot{Q}$ is the heat flow, t_0 and t_1 is the time point of the start and the end of the phase transition respectively.

First-principle DFT calculation for gas adsorption

The initial crystal structure of LS-1 and HS were imported from the.cif files of the experimental crystal, C 2/c space group with a = 21.0725 Å, b = 10.0692 Å, c = 12.1339 Å, $\alpha = \gamma = 90°$ and β = 102.9826° for LS-1, and a = 22.801Å, b = 9.917Å, c = 11.686Å, $\alpha = \gamma = 90°$, and β = 106.47° for HS. The imported crystal was then fully optimized using the Quantum ESPRESSO (v.7.3.1) software[62,63] with all four independent Fe(II) ions in each unit cell being at high spin state (HS) and at low spin state (LS-1), respectively for simulation. In addition, to simulate the extra pressure-induced N_2 insertion, N_2 molecules were inserted randomly into the crystal unit cell. For all calculations, electron-ion interactions were described with scalar-relativistic optimized norm-conserving Vanderbilt (ONCV) pseudopotentials[64,65]. The kinetic cutoff energy for the wave functions was set to 80 Ry. The generalized gradient approximation (GGA) of Perdew, Burke, and Ernzerhof (PBE)[66] was used.

Data availability

The main data supporting the findings of this study are available within the paper and its Supplementary Information. Considering the huge quantity of raw data, all raw data generated during the current study are available from the corresonding author (F.X.H. fxhu@iphy.ac.cn) upon request.

References

1. Purohit, P. et al. Electricity savings and greenhouse gas emission reductions from global phase-down of hydrofluorocarbons. *Atmos. Chem. Phys.* **20**, 11305–11327 (2020).
2. Abas, N. et al. Natural and synthetic refrigerants, global warming: a review. *Renew. Sustain. Energy Rev.* **90**, 557–569 (2018).
3. She, X. et al. Energy-efficient and -economic technologies for air conditioning with vapor compression refrigeration: a comprehensive review. *Appl. Energy* **232**, 157–186 (2018).

4. Stern, P. C. et al. Opportunities and insights for reducing fossil fuel consumption by households and organizations. *Nat. Energy* **1**, 16043 (2016).
5. McLinden, M. O., Brown, J. S., Brignoli, R., Kazakov, A. F. & Domanski, P. A. Limited options for low-global-warming-potential refrigerants. *Nat. Commun.* **8**, 14476 (2017).
6. Velders, G. J. M., Fahey, D. W., Daniel, J. S., McFarland, M. & Andersen, S. O. The large contribution of projected HFC emissions to future climate forcing. *Proc. Natl. Acad. Sci. USA* **106**, 10949–10954 (2009).
7. Henry, A., Prasher, R. & Majumdar, A. Five thermal energy grand challenges for decarbonization. *Nat. Energy* **5**, 635–637 (2020).
8. Mañosa, L. & Planes, A. Solid-state cooling by stress: a perspective. *Appl. Phys. Lett.* **116**, 050501 (2020).
9. Lin, Y. et al. A full solid-state conceptual magnetocaloric refrigerator based on hybrid regeneration. *Innovation* **5**, 100645 (2024).
10. Biswas, A. et al. Designed materials with the giant magnetocaloric effect near room temperature. *Acta Materialia* **180**, 341–348 (2019).
11. Terada, N. & Mamiya, H. High-efficiency magnetic refrigeration using holmium. *Nat. Commun.* **12**, 1212 (2021).
12. Zhang, Z. et al. Intense ferromagnetic fluctuations preceding magnetoelastic first-order transitions in giant magnetocaloric $LaFe_{13-x}Si_x$. *Phys. Rev. Mater.* **5**, L071401 (2021).
13. Guillou, F. et al. Non-hysteretic first-order phase transition with large latent heat and giant low-field magnetocaloric effect. *Nat. Commun.* **9**, 2925 (2018).
14. Wang, Y. et al. A high-performance solid-state electrocaloric cooling system. *Science* **370**, 129–133 (2020).
15. Nouchokgwe, Y. et al. Giant electrocaloric materials energy efficiency in highly ordered lead scandium tantalate. *Nat. Commun.* **12**, 3298 (2021).
16. Park, M. H. et al. Giant negative electrocaloric effects of $Hf_{0.5}Zr_{0.5}O_2$ thin films. *Adv. Mater.* **28**, 7956–7961 (2016).
17. Torelló, A. et al. Giant temperature span in electrocaloric regenerator. *Science* **370**, 125–129 (2020).
18. Tušek, J. et al. A regenerative elastocaloric heat pump. *Nat. Energy* **1**, 16134 (2016).
19. Yang, Z., Cong, D. Y., Sun, X. M., Nie, Z. H. & Wang, Y. D. Enhanced cyclability of elastocaloric effect in boron-microalloyed Ni-Mn-In magnetic shape memory alloys. *Acta Materialia* **127**, 33–42 (2017).
20. Hou, H. et al. Fatigue-resistant high-performance elastocaloric materials made by additive manufacturing. *Science* **366**, 1116–1121 (2019).
21. Gao, Y.-H. et al. Low pressure reversibly driving colossal barocaloric effect in two-dimensional vdW alkylammonium halides. *Nat. Commun.* **15**, 1838 (2024).
22. Yu, Z. et al. Colossal barocaloric effect achieved by exploiting the amorphous high entropy of solidified polyethylene glycol. *NPG Asia Mater.* **14**, 96 (2022).
23. Gao, Y. et al. Reversible colossal barocaloric effect dominated by disordering of organic chains in $(CH_3–(CH_2)_{n-1}–NH_3)_2MnCl_4$ single crystals. *NPG Asia Mater.* **14**, 34 (2022).
24. Wu, R.-R. et al. Giant barocaloric effect in hexagonal Ni_2In-type Mn-Co-Ge-In compounds around room temperature. *Sci. Rep.* **5**, 18027 (2015).
25. Li, B. et al. Colossal barocaloric effects in plastic crystals. *Nature* **567**, 506–510 (2019).
26. Lloveras, P. et al. Colossal barocaloric effects near room temperature in plastic crystals of neopentylglycol. *Nat. Commun.* **10**, 1803 (2019).
27. Piper, S. L. et al. Organic ionic plastic crystals having colossal barocaloric effects for sustainable refrigeration. *Science* **387**, 56–62 (2025).
28. Lin, J. et al. Colossal and reversible barocaloric effect in liquid-solid-transition materials n-alkanes. *Nat. Commun.* **13**, 596 (2022).
29. Aznar, A. et al. Reversible and irreversible colossal barocaloric effects in plastic crystals. *J. Mater. Chem. A* **8**, 639–647 (2020).
30. Sandeman, K. G. Research Update: the mechanocaloric potential of spin crossover compounds. *APL Mater.* **4**, 111102 (2016).
31. Gütlich, P., Hauser, A. & Spiering, H. Thermal and optical switching of iron(II) complexes. *Angew. Chem. Int. Ed. Engl.* **33**, 2024–2054 (1994).
32. König, E. Nature and dynamics of the spin-state interconversion in metal complexes. In *Complex Chemistry* 51–152 https://doi.org/10.1007/3-540-53499-7_2 (Springer, 1991).
33. Real, J. A., Gaspar, A. B., Niel, V. & Muñoz, M. C. Communication between iron(II) building blocks in cooperative spin transition phenomena. *Coord. Chem. Rev.* **236**, 121–141 (2003).
34. Spin Crossover in *Transition Metal Compounds I*. vol. 233 (Springer, 2004).
35. Real, J. A., Gaspar, A. B. & Muñoz, M. C. Thermal, pressure and light switchable spin-crossover materials. *Dalton Trans.* 2062–2079 https://doi.org/10.1039/B501491C (2005).
36. Hauser, A. Spin-crossover materials properties and applications. *Angew. Chem. -Int. Ed.* **52**, 10419–10419 (2013).
37. Rat, S. et al. Coupling mechanical and electrical properties in spin crossover polymer composites. *Adv. Mater.* **30**, 1705275 (2018).
38. Li, B. et al. Sophisticated construction of electronically labile materials: a neutral, radical-rich, cobalt valence tautomeric triangle. *J. Am. Chem. Soc.* **140**, 14581–14585 (2018).
39. Li, B. et al. Unconventional method for fabricating valence tautomeric materials: integrating redox center within a metal–organic framework. *J. Am. Chem. Soc.* **141**, 6822–6826 (2019).
40. Zhang, L. et al. Anomalous light-induced spin-state switching for iron(II) spin-crossover molecules in direct contact with metal surfaces. *Angew. Chem. -Int. Ed.* **59**, 13341–13346 (2020).
41. Vallone, S. P. et al. Giant barocaloric effect at the spin crossover transition of a molecular crystal. *Adv. Mater.* **31**, 1807334 (2019).
42. Seo, J., Braun, J. D., Dev, V. M. & Mason, J. A. Driving barocaloric effects in a molecular spin-crossover complex at low pressures. *J. Am. Chem. Soc.* **144**, 6493–6503 (2022).
43. von Ranke, P. J. et al. Colossal refrigerant capacity in [Fe(hyptrz)3] A2 • H2O around the freezing temperature of water. *Phys. Rev. B* **98**, 224408 (2018).
44. Li, R. et al. Colossal barocaloric effect of the spin-crossover compound {Fe(pz)2(BH3CN)2} near room temperature. *Appl. Phys. Lett.* **124**, 122202 (2024).
45. Ohkoshi, S. et al. Giant adiabatic temperature change and its direct measurement of a barocaloric effect in a charge-transfer solid. *Nat. Commun.* **14**, 8466 (2023).
46. Lunser, K. et al. Elastocaloric, barocaloric and magnetocaloric effects in spin crossover polymer composite films. *Nat. Commun.* **15**, 6171 (2024).
47. Lloveras, P. *Barocaloric Effects in the Solid State: Materials and Methods*. (IOP Publishing, 2023).
48. Yu, H. et al. The low-pressure-driven barocaloric effect at room temperature in the two-dimensional hofmann-type coordination polymer {FeII(pdz)2[Pt(CN)4]}. *Inorg. Chem.* **65**, 2045–2054 (2026).
49. Vela, S. et al. Atomistic description of spin crossover under pressure and its giant barocaloric effect. *J. Mater. Chem. C.* **13**, 19635–19641 (2025).
50. Gracia, D. et al. Room-temperature barocaloric effect in [Fe(pap-5NO2)2] spin-crossover material. *J. Mater. Chem. A* **13**, 17944–17951 (2025).
51. Seredyuk, M. et al. Reversible colossal barocaloric effect of a new feii molecular complex with low hysteretic spin crossover behavior. *Adv. Funct. Mater.* **34**, 2315487 (2024).
52. Romanini, M. et al. Giant and reversible barocaloric effect in trinuclear spin-crossover complex Fe3(bntrz)6(tcnset)6. *Adv. Mater.* **33**, 2008076 (2021).

53. Zhang, L. et al. Abrupt spin transition around room temperature and light induced properties in Fe^{II} complexes with N_4O_2 coordination sphere. *Chem. Commun.* **46**, 2554 (2010).
54. MASON, J. A., SEO, J. & Slavney, A. H. Inverted barocaloric effects. WO2024081374A1 (2024).
55. Szilágyi, P. Á et al. Temperature and pressure effects on the spin state of ferric ions in the [Fe(sal2-trien)][Ni(dmit)2] spin crossover complex. *J. Phys. Chem. Solids* **69**, 2681–2686 (2008).
56. Moya, X., Kar-Narayan, S. & Mathur, N. D. Caloric materials near ferroic phase transitions. *Nat. Mater.* **13**, 439–450 (2014).
57. Aznar, A. et al. Giant barocaloric effects over a wide temperature range in superionic conductor AgI. *Nat. Commun.* **8**, 1851 (2017).
58. Wang, X. et al. Colossal barocaloric effect with a wide working-temperature span in octylamine hydrochloride. *J. Mater. Chem. A* **13**, 1399–1406 (2025).
59. Seo, J. et al. Colossal barocaloric effects with ultralow hysteresis in two-dimensional metal–halide perovskites. *Nat. Commun.* **13**, 2536 (2022).
60. Hobday, C. L. et al. Understanding the adsorption process in ZIF-8 using high pressure crystallography and computational modelling. *Nat. Commun.* **9**, 1429 (2018).
61. Moggach, S. A., Bennett, T. D. & Cheetham, A. K. The effect of pressure on ZIF-8: increasing pore size with pressure and the formation of a high-pressure phase at 1.47 GPa. *Angew. Chem. -Int. Ed.* **48**, 7087–7089 (2009).
62. Giannozzi, P. et al. QUANTUM ESPRESSO: a modular and open-source software project for quantum simulations of materials. *J. Phys. Condens. Matter* **21**, 395502 (2009).
63. Giannozzi, P. et al. Advanced capabilities for materials modelling with Quantum ESPRESSO. *J. Phys. Condens. Matter* **29**, 465901 (2017).
64. Hamann, D. R. Optimized norm-conserving Vanderbilt pseudopotentials. *Phys. Rev. B* **88**, 085117 (2013).
65. Schlipf, M. & Gygi, F. Optimization algorithm for the generation of ONCV pseudopotentials. *Computer Phys. Commun.* **196**, 36–44 (2015).
66. Perdew, J. P., Burke, K. & Ernzerhof, M. Generalized gradient approximation made simple. *Phys. Rev. Lett.* **77**, 3865–3868 (1996).
67. Zhang, K. et al. Colossal Barocaloric effect in carboranes as a performance tradeoff. *Adv. Funct. Mater.* **32**, 2112622 (2022).
68. Bermúdez-García, J. M. et al. Giant barocaloric effect in the ferroic organic-inorganic hybrid [TPrA][Mn(dca)$_3$] perovskite under easily accessible pressures. *Nat. Commun.* **8**, 15715 (2017).
69. Salvatori, A. et al. Large barocaloric effects in two novel ferroelectric molecular plastic crystals. *J. Mater. Chem. A* **11**, 12140–12150 (2023).
70. García-Ben, J. et al. Unveiling barocaloric potential in organometallic-sandwich compounds [Cp_2M][PF_6] (M: Fe^{3+}, Co^{3+}). *J. Mater. Chem. A* **12**, 23751–23760 (2024).
71. Aznar, A. et al. Giant and reversible inverse barocaloric effects near room temperature in ferromagnetic $MnCoGeB_{0.03}$. *Adv. Mater.* **31**, 1903577 (2019).
72. Lloveras, P. et al. Giant barocaloric effects at low pressure in ferrielectric ammonium sulphate. *Nat. Commun.* **6**, 8801 (2015).
73. Li, J. et al. Reversible barocaloric effects over a large temperature span in fullerite C_{60}. *J. Mater. Chem. A* **8**, 20354–20362 (2020).
74. Ren, Q. et al. Ultrasensitive barocaloric material for room-temperature solid-state refrigeration. *Nat. Commun.* **13**, 2293 (2022).

Author contributions

F.X.H. and B.G.S. formulated the project. S.M. and D.P.Z. synthesized the sample. Y.K. and S.W.Y. collected and analyzed the pressure calorimetry data. Y.K. constructed the small pressure VP-PXRD device equipped on SSRF with help of Y.R. and L.J.W. R.X.L. and Y.K. performed the VP-PXRD and VP/VT-Raman experiment. Q.Z.H., I.S., J.W., and Z.Y.T. provided constructive viewpoints about the PXRD results. Z.L.Z. provided help for the SR-PXRD experiment. C.Q.J. provided suggestions for the analysis of Raman experiments. Y.X.Z. performed the first-principle DFT calculations. D.P.Z., Z.Y.T., Q.Z.H., Q.J.L., Y.S.C., Y.Z.C., Y.X.Z., J.W., H.L., J.Y.L., V.F., and O.G. contributed to data analysis and discussion. Y.K. and F.X.H. wrote the paper with input from all coauthors.

Funding

This work was supported by the National Key Research and Development Program of China (Grant No. 2023YFA1406003 (C.Q.J. and F.X.H.)), the National Natural Sciences Foundation of China (Grant Nos. 52688201 (B.G.S.), 92263202 (F.X.H.), U23A20550 (F.X.H.), 22171166 (D.P.Z.), 12595332 (Y.S.C.), 22361132534 (J.W. and F.X.H.), U25A6010 (J.W.)), the Strategic Priority Research Program B (XDB1270201 (F.X.H.), XDB1720000 (Y.S.C.)) of Chinese Academy of Sciences (CAS). A portion of this work was carried out at the Synergetic Extreme Condition User Facility (SECUF) and beamline BL12SW in Shanghai Synchrotron Radiation Facility (SSRF). V.F. and J.Y.L. acknowledge the support of AEI/FEDER-UE (grant PID2023-146047OB-I00 (V.F. and J.Y.L.) from AEI/10.13039/501100011033), and of the Chinese Academy of Sciences President's International Fellowship Initiative (PIFI) for visiting scientists (Grants Nos. 2024VMA0021(V.F.), 2024VMC0006(J.Y.L.)). J.Y.L. acknowledges EMERGIA Fellowship (EMC21_00418) from Junta de Andalucía.

Competing interests

The authors declare no competing interests.

Additional information

Supplementary information The online version contains supplementary material available at https://doi.org/10.1038/s41467-026-77679-7.

Correspondence and requests for materials should be addressed to Jing Wang, Dao-Peng Zhang, Feng-Xia Hu or Bao-Gen Shen.

Peer review information *Nature Communications* thanks the anonymous reviewer(s) for their contribution to the peer review of this work. A peer review file is available.

Reprints and permissions information is available at http://www.nature.com/reprints

Publisher's note Springer Nature remains neutral with regard to jurisdictional claims in published maps and institutional affiliations.

Open Access This article is licensed under a Creative Commons Attribution-NonCommercial-NoDerivatives 4.0 International License, which permits any non-commercial use, sharing, distribution and reproduction in any medium or format, as long as you give appropriate credit to the original author(s) and the source, provide a link to the Creative Commons licence, and indicate if you modified the licensed material. You do not have permission under this licence to share adapted material derived from this article or parts of it. The images or other third party material in this article are included in the article's Creative Commons licence, unless indicated otherwise in a credit line to the material. If material is not included in the article's Creative Commons licence and your intended use is not permitted by statutory regulation or exceeds the permitted use, you will need to obtain permission directly from the copyright holder. To view a copy of this licence, visit http://creativecommons.org/licenses/by-nc-nd/4.0/.

© The Author(s) 2026